Segregation of hydrogen and vacancies at the Σ5(210)[001] symmetric tilt grain boundary in Ni and influence on cohesion

X. J Shen, D. Connétable, E. Andrieu, Döme Tanguy

Segregation of hydrogen and vacancies at the $\Sigma5(210)[001]$ symmetric tilt grain boundary in Ni and influence on cohesion.

X. J. Shen[1,2], D. Connétable[3], E. Andrieu[3] and D. Tanguy[1]

[1] Institut Lumière Matière, UMR5306 Université Lyon 1 - CNRS, Université de Lyon 69622 Villeurbanne cedex, France

[2] Engineering Research Center of Advanced Functional Material Manufacturing of Ministry of Education, Zhengzhou University, Zhengzhou 450001, People's Republic of China

[3] CIRIMAT, CNRS, Toulouse, France, CIRIMAT-ENSIACET, 4 allé Émile Monso, BP 44362, F-31030 Toulouse Cedex 4, France

E-mail: `dome.tanguy@univ-lyon1.fr`

August 2020

Abstract. The segregation of hydrogen and vacancies at the $\Sigma5(210)[001]$ symmetric tilt grain boundary (GB) was studied by atomic scale simulations in Ni. First, the hydrogen segregation energies and hydrogen-hydrogen pair interaction energies were calculated on every interstitial site of the GB. The vacancy-hydrogen clusters' formation energies were also determined on the most favorable site. All these calculations were done using the Density Functional Theory (DFT). Second, based on these elementary energies, a free energy functional was built to determine the concentration of segregated hydrogen and of vacancy-hydrogen clusters, as a function of the bulk hydrogen concentration and the temperature. It was found that two configurations exits in typical conditions where embrittlement is observed experimentally: H segregation only, with up to 3 hydrogen atom per structural unit or 50% occupancy by VH_5 clusters (1 cluster every two structural unit). The cohesive stress and ideal work of fracture were evaluated by fracturing the GB with different degrees of hydrogen and vacancy segregation. H segregation alone (no vacancy) decreased the work of fracture by 25%. A significantly larger decrease of cohesion was obtained when considering vacancy-hydrogen clusters. A maximum drop of the cohesive stress, of a magnitude of 40%, was obtained when every structural unit was hosting a VH_4 cluster. Finally, these data were transformed into cohesive stress models. They were used to evaluate the degree of localization of the shear displacement at the crack tip. The conclusion is that, even if cohesion is very significantly decreased, shear localization is still effective, meaning that dislocation emission should occur at the expense of crack propagation. Therefore, extra ingredients should be considered to explain the embrittlement observed experimentally.

Submitted to: *Modelling Simul. Mater. Sci. Eng.*

1. Introduction

Hydrogen embrittlement of metals is an important issue because it causes crack initiation and propagation at low load levels and at high speeds and is therefore potentially dangerous. A large research effort has been dedicated to characterizing the phenomenon in all sorts of metallic alloys and environments [1–6]. A number of models have been proposed [7; 8] based on fractography [7], in situ acoustic emission [9; 10] or in situ TEM [11]. The origin of the embrittlement remains unclear. Four microscopic mechanisms were proposed : decohesion (transgranular cleavage or separation along the core of grain boundaries), enhanced crack tip plasticity due to hydrogen adsorption, enhanced and localized plasticity ahead of the tip [11–14] and, more recently, aggregation of hydrogen stabilized vacancies [15; 16]. Some aspects of these mechanisms have been more precisely quantified by modern experimental techniques, with high spatial resolutions. For example, the trapping of hydrogen at interfaces has been demonstrated, at the atomic scale, by atom probe tomography [17] and a dislocation substructure with a typical length scale of 250 nm was imaged in the plastic wake, below the fracture surface [18; 19]. Small scale mechanical testing also produced new in situ observations, such as, the confinement of the plastic zone (50 nm) during transgranular cracking in bending micro beams [20] in FeAl, or the locking of dislocations by vacancy-hydrogen clusters using a cyclic compression of a nano pillar in a TEM [3]. Note the recent observations of the cracking of bcc Fe at low temperature [21; 22] which reveal a mixture of cleavage and localized plasticity and the critical review of the limitations of current atomistic simulations of dislocation emission at crack tips in bcc Fe [23]. They constitute a reference for the hydrogen embrittlement of steels at room temperature.

The efforts made by the modeling community in trying to validate or invalidate such micro-mechanisms have been intense and now covers all the different aspects. Adsorbed, or sub-surface, hydrogen does not seem to enhance dislocation emission at crack tips, at least in Al [24–26]. Intergranular diffusion, where both speed up and slow down have been measured experimentally, seems to be well understood [27–30], especially the H concentration effect. Preliminary results on pipe diffusion were also recently reported [31]. The effect of co-segregation has been intensively studied [32], in particular at the interface between carbides and the bcc-Fe matrix [33]. Concerning vacancies [15], the origin of the enhancement of their concentration is the strong binding between hydrogen atoms and vacancies and the possibility of multiple occupation [34–37]. They also impact diffusion [38; 39], but in conditions which might not be those of embrittlement, at least if vacancies are considered in equilibrium with H. The impact of hydrogen on the mobility of screw dislocations in Fe, a key issue for the embrittlement of steels, has been modeled recently [14].

The most important aspect is fracture itself. In hydride forming systems, the crack tip, with its stress concentration and layer of adsorbed H, might act as a seed for stabilizing a local hydride, which will prevent the tip to relax by emitting dislocations and therefore promote brittle fracture [40]. In non-hydride forming systems, the Rice and

Wang model [41], with parameters from Density Functional Theory (DFT) calculations, shows that beyond a critical chemical H potential, a phase transition occurs where, at a critical applied stress, the opening interface becomes abruptly fully populated by H. When this occurs, the cohesive stress is drastically reduced [42]. A kinetic version of this model was recently proposed for the embrittlement of grain boundaries in Ni [43]. In contrast, when the local H concentration is kept fixed during fracture, hydrogen's impact is weak: configurations which were initially ductile, i.e. with a glide plane properly oriented with respect to the crack tip for an easy activation of plasticity, remain ductile in the presence of segregated hydrogen, even if the concentration is representative of experiments [44]. In contrast, the cohesion never drops to zero because of hydrogen charging in experiments, at least in Ni, and crack propagation occurs, even along grain boundaries, with intense plastic deformation [18]. Therefore, some extra mechanisms should be considered in between the two extremes of the absence of diffusion during fracture and an instantaneous diffusion of H to the surface.

One way, in the intergranular case, is to complexify the grain boundary configurations by considering vacancies in addition to hydrogen. The driving force for stabilizing them is the same as in the bulk but, with a lower formation energy at grain boundaries, large concentrations of vacancies can be expected. A first study in this direction was done on the $\Sigma3\{112\}\langle110\rangle$ symmetrical tilt grain boundary (GB) of bcc Fe. Intergranular vacancies were found to significantly decrease the work of fracture, with respect to hydrogen alone [45]. Nevertheless, a limitation of this work is the lack of a clear connection of the local H and vacancy concentrations to experimental conditions.

In this context, the goal of the paper is to model realistic GB configurations in the presence of segregated hydrogen and vacancies. The method is first to obtain H segregation energies and vacancy-hydrogen cluster (VH_n, n H for one vacancy) formation energies in the GB from reliable electronic structure calculations. These energies are then introduced in a free energy functional which gives the average concentration of H on the various interstitial sites of the GB and the VH_n concentrations as a function of the thermodynamic parameters c_{bulk} (the H concentration of regular bulk interstitial sites) and the temperature T. Finally, atomic configurations representative of the experimental conditions for H embrittlement are chosen and fractured. The influence of H and VH_n on cohesion is quantified. The system chosen is Ni because there are numerous observations of intergranular embrittlement [18] and because vacancy effects were observed [46].

The paper is organized as follows. The construction of the GB and the methods are first described. Then, the structure of the GB and the formation energies of the vacancies are detailed. The segregation energies of isolated hydrogen atoms and the formation energy of the various clusters on the most favorable site of the GB are given. The hydrogen-hydrogen pair interaction energies are determined. Then, these data are used to parametrize a free energy functional which minimization gives the hydrogen concentration on regular interstitial sites. As the bulk concentration is increased the grain boundary becomes occupied by vacancy-hydrogen clusters. Finally, representative GB structures with hydrogen segregation alone, or with segregated vacancy-hydrogen

clusters are selected and fractured along the interface plane. The absence of impact of the vacancies on the ideal work of fracture, compared to the effect of H alone, is discussed.

2. Models and Methods

2.1. Grain boundary model

The Coincidence Site Lattice (CSL) was used for the construction of the Σ5(210)[001] symmetrical tilt grain boundary. After the elimination of overlapping atoms in the GB plane and relaxation of stresses and forces, the minimal energy structure was obtained. Each CSL unit contains two equivalent GB structural units, as shown in the figure 1a. Characteristic atomic sites are labeled GB_1, GB_2 and GB_3. The x axis is oriented along [210], y along [$\bar{1}$20] and z along [001]. Two system sizes were used: one with only one CSL unit on each side of the GB and two periods along the tilt axis (z) (80 atoms) and a second one, elongated in the x direction (112 atoms) (Fig. 1). Periodic boundary conditions were imposed in the y and z directions. In the x direction, free surfaces were

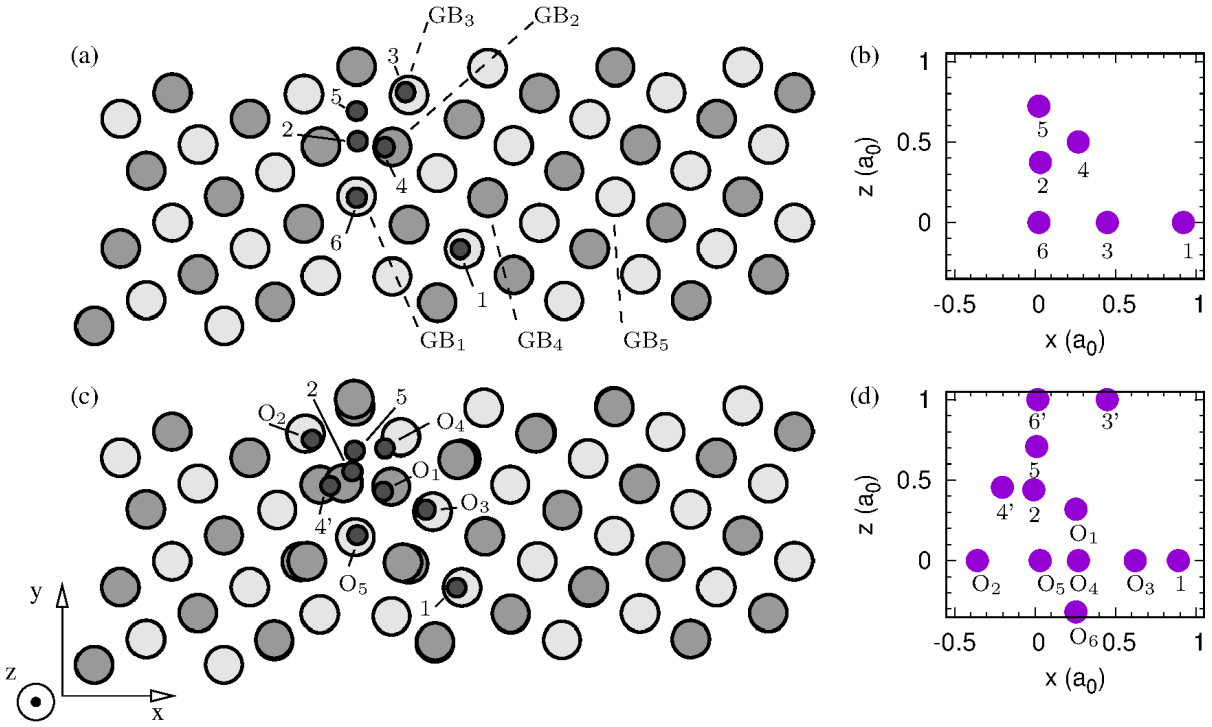

Figure 1. (a) and (b) show the GB structural units and interstitial positions in the (x,y) plane and (x,z) planes respectively. (c) and (d) give the same information for a GB containing a single vacancy on a GB_2 site on the (x¿0) side of the interface, i.e. the plane is occupied by 25% of vacancies (the box contains 4 structural units). Note the relaxation towards the interface of the GB_2 site, from the left grain, symmetric of the vacancy.

created by introducing a vacuum layer of thickness 7.0 Å. The surface layers are held

rigid, at the perfect lattice parameter to mimic bulk behavior. In the small system, the rigid part starts beyond the seventh (210) layer, while in the enlarged region of the big system, it starts after the sixteenth layer. The box size was optimized in the x direction, while keeping the bulk lattice parameter in the other directions.

In the perfect face centered cubic (fcc) structure, which is the most stable for Ni, there are two tetrahedral and one octahedral sites for each fcc lattice site. Such interstitial sites were geometrically constructed, by displacement from the lattice site, for every atom of the left grain, including the sites of the GB plane. Then they were transformed by a planar symmetry with respect to the interface plane and used for the atoms of the right grain, including again the atoms of the GB plane. This procedure creates a high density of geometric interstitial sites in the core of the GB. Searching for the metastable sites for H segregation, 15 of such geometric sites were used as starting points. Many of them relaxed to the same configuration.

2.2. Density Functional Theory Calculations

In order to obtain reliable equilibrium atomic structures of GBs and accurate hydrogen segregation energies first-principles calculations were conducted to optimize structures and calculate system energies. Our calculations were performed within the density functional theory (DFT) and carried out with the generalized gradient approximations (GGA) to the exchange-correlation functional (Perdew-Burke-Ernzerhof –PBE– functional) [47], as implemented in the Vienna Ab initio Simulation Package (VASP) [48]. We used projector-augmented wave (PAW) [49] method for valence electrons and a 1×3×3 **k**-points grid for the Brillouin zone sampling. Spin-polarization effects for all the considered system were taken into account. Plane-waves were used for expanding the wave functions with a cutoff energy equal to 400 eV. These criteria are necessary when optimizing atomic forces ($<$ 0.01 eV/Å) and obtain accurate energies ($<$2-4 meV).

The zero-point vibrational energy (ZPE) of H atoms was computed for all Ni-H systems we selected. In calculating the zero-point vibrational energy of hydrogen atom in the Ni-H system, the dynamical matrix only for H atoms using the frozen phonon approach (the relative displacements was taken equal to 0.01 Å) was used to calculate the vibrational frequency. Using the real frequencies of hydrogen (ω_n), we calculated the ZPE of H atoms, where the ZPE is approximated by $ZPE = \Sigma_n \hbar\omega_n/2$ at 0 K.

2.3. Mean Field Equations

The average hydrogen and vacancy concentrations in the GB are calculated using a free energy functional. Its simplest form, with hydrogen only, is detailed here. It will be complexified later to introduce also vacancies. In the case of hydrogen alone, the variables of the functional are the concentrations on every interstitial site (c_i) and the parameters are the temperature (T) and the hydrogen chemical potential (μ_H). Its optimization gives the equilibrium concentrations on the interstitial sites of the GB. A

first, approximate, mean internal energy can be obtained from the segregation energies on each site i of the GB (ΔE^i_{seg}), defined in the absence of interactions between the occupied sites (dilute limit). As will appear clearly below, the specificity of the GB core requires that the H-H interactions are included in the model. This is done by calculating effective pair-interactions by taking the energy difference between two configurations containing two H atoms: the final one in which the two H atoms are close and the reference one in which each solute occupies its GB interstitial site, but far enough so that the interaction between them can be neglected. In DFT calculations, because of the size limitation, a reference energy (E'_{ref}) is calculated with one H atom on its GB interstitial site (for example site j) and the second one on a bulk site. By using the value of the segregation energy on site i, the effective pair interaction ϵ_{ij} between interstitial sites i and j is then defined by [37]:

$$\epsilon_{ij} = E_{ij} - (E'_{ref} + \Delta E^i_{seg}) \tag{1}$$

where E_{ij} is the energy of the configuration where the sites i and j are occupied. With these parameters, the free energy, as a function of the average occupancy of the GB sites c_i and the bulk sites c_{bulk}, is:

$$\begin{aligned} F_{N_H,V,T}(c_i) = E_0 + \sum_i \{ & c_i \Delta E^i_{seg} + \sum_j c_i c_j \epsilon_{ij} \\ & + k_B T (c_i \ln c_i + (1-c_i)\ln(1-c_i))\} \end{aligned} \tag{2}$$

The constraint of a fixed number of H atoms, N_H, is taken into account by introducing a Lagrange multiplier μ_H. Writing the optimization condition for each kind of site gives the equilibrium concentrations:

$$\begin{aligned} \frac{c_i}{1-c_i} &= e^{-(\Delta E^i_{seg} + \sum_j c_j \epsilon_{ij} - \mu_H)/k_B T} \\ \frac{c_{bulk}}{1-c_{bulk}} &= e^{\mu_H / k_B T} \end{aligned} \tag{3}$$

where c_{bulk} is the H concentration on a bulk site (far from the GB). The equations, and approximations, specific to the GB structure are given in section 3.4.

3. Results

3.1. Atomic structure of the grain boundary and vacancy formation energies

The vacancy formation energy is evaluated on every site of the GB. In the case of a system containing n vacancies, the excess energy E^f_n, per vacancy (the average formation energy) is:

$$E^f_{nv} = (E_{defect} + n\ E_{bulk} - E_{perfect})/n \tag{4}$$

where $E_{perfect}$ is the energy of the reference structure (the one with the minimum energy) shown on Fig. 1a, E_{bulk} is the energy of a Ni atom in a perfect crystal. It is calculated using a cell containing 4 Ni atoms and a 9×9×9 k point mesh. The atomic energy is -5.571 eV/atom. E_{defect} corresponds to the energy of the system containing n vacancies.

Table 1. Positions (in a_0) and vacancy formation energies E^f_{nv} (in eV) obtained by DFT for the large (small) GB structures.

site	x	y	z	E^f_{1v}	E^f_{2v}
GB_1	0.023	1.120	-0.500	(1.843)	1.432
GB_2	0.334	1.547	0.000	0.210 (-0.100)	0.075
GB_3	0.475	1.994	-0.500	(1.143)	1.207
GB_4	1.155	1.110	0.000	0.972 (0.968)	1.032
GB_5	2.472	1.565	0.000	1.313	

In bulk Ni, with the same DFT parameters, the vacancy formation energy is about 1.40 eV [50], in good agreement with other theoretical values [35] (1.44 eV). It has been recently shown that the long standing discrepancy between the experimental values of the free formation energy obtained at high temperature and the low temperature values from DFT can be explained by an-harmonic effects [51]. Therefore, we take 1.40 eV as a reference value for the formation energy in the bulk.

After relaxation, the perfect Ni-Σ5(210)[001] symmetrical tilt GB remains symmetric. The single vacancy formation energy E^f_{1v} was calculated on every GB site and gave the following values, for the small system: 1.843, -0.100 and 1.143 eV for sites GB_1, GB_2 and GB_3 respectively and on the most remote site, GB_4, 0.968 eV. The value on GB_4 is significantly different from the bulk one and therefore, this site is too close to the GB to be used as a reference for the vacancy segregation energies. Furthermore, with this system size, the perfect GB is unstable with respect to the formation of vacancies (the formation energy on site GB_2 is negative). The "large" system (Fig. 1) is asymmetric in order to contain sites further away from the GB with still an affordable computational effort. E^f_{1v} on one of such sites, GB_5, is 1.313 eV, closer to the bulk calculation (1.400 eV). It is therefore used as a reference site for segregation energies. With this system size, the vacancy formation energies on sites GB_2 and GB_4 are respectively: 0.210 eV and 0.972 eV. The other sites are not considered any longer because the formation energy, there is too high to lead to vacancy-H clusters in the thermodynamic conditions considered here. The symmetric GB is now stable with respect to vacancy formation (all formation energies are now significantly higher than 0). Note the large relaxation induced by the vacancy (Fig. 1c), especially the displacement of the occupied GB_2 site (left side of the GB) towards the interface plane.

In addition to single vacancies, we also studied divacancies aligned along the tilt axis. Because of the short dimension of the system in this direction, which corresponds to only two equivalent sites, and the periodic boundary conditions, the divacancy is in fact an infinite line of vacancies. The average formation energy per vacancy E^f_{2v} for sites GB_1, GB_2 GB_3 and GB_4 are respectively: 1.432 eV, 0.075 eV, 1.207 eV and 1.032 eV. Again, the reference GB structure is stable, even if removing a line of GB_2 sites creates a GB with an energy very similar to the reference. All vacancy formation energies are listed in Table 1 with the corresponding site positions.

3.2. Intergranular hydrogen segregation energies, effect of vacancies

For calculating the hydrogen segregation energies, a reference was created by placing the H atom as far from the GB as possible, in octahedral position. Then a series of DFT calculations were conducted on configurations where the solute was placed at the different geometrical interstitial sites in the GB core and relaxed, as discussed in subsection 2.1. The segregation energy (ΔE^i_{seg}) is the difference between such configurations, labeled i, and the reference:

$$\Delta E^i_{seg} = E_{jdg}(H^i) - E_{jdg}(H^{octa}) \tag{5}$$

where $E_{jdg}(H^i)$ and $E_{jdg}(H^{octa})$ are the energy of an H atom occupying the i site of the GB and the energy of an H atom in a bulk octahedral site. A negative ΔE^i_{seg} (resp. positive) value means an enrichment (resp. a depletion) with respect to the bulk. Only 5 different metastable positions were found after minimization, with DFT. They were presented on Fig. 1a. The corresponding segregation energies are given in Table 2, as well as the positions. The zero-point energy corrections are also listed in Table 2. In bulk Ni, the octahedral and tetrahedral sites have a large energy difference, of the order of 0.22 eV [50], with the first one being the most stable. In the GB, the most stable position for hydrogen is also an octahedral site (site 6). The corresponding segregation energy is -0.244 eV (resp. -0.278) without (resp. with) the ZPE correction. The second deepest trap site is site 5 (-0.266 eV), which is tetrahedral and the third one is site 4 (-0.182 eV). These results are in good agreement with other DFT calculations [29; 52]. Site 1 is already a bulk site, which indicates that the influence of the GB is short range.

Next, a vacancy is created on the GB site with the lowest vacancy formation energy: site GB_2. It has two effects on the segregation sites for H: it modifies the existing sites and it creates new ones (see Fig. 1 c and d). Because the system contains two cells along the tilt axis, removing one atom creates a concentration of vacancies of 50% on the GB_2 sites along the tilt axis. As a consequence, the interstitial sites are not always equivalent along the tilt axis direction anymore. The structural units are also no longer equivalent along the y axis. Nevertheless, we did not evaluate the impact of the vacancy on the H segregation energies on these structural units which are relatively remote from the vacancy. We expect the modifications to be minor. First, the two core interstitial sites, 2 and 5 (tetrahedral) are largely affected. Trapping is reinforced on the first one ($\Delta E^{2\ ZPE}_{seg} = -0.210$ eV vs. -0.134 eV without vacancy) and decreased on the second one ($\Delta E^{5\ ZPE}_{seg} = -0.193$ eV vs. -0.266 eV without vacancy). Second, there are 6 octahedral sites in first neighboring position of the vacancy (the O_1 sites of the bulk vacancy [50]). Four of them are at the same z position as site GB_2: O_2,O_4,O_5 and O_3. They replace respectively the sites 3' (the symmetric of site 3), 3 and 6. Site O_3 is a new strong trap site. All the sites of the vacancy lead to a re-enforcement of trapping (Tab. 2), especially site O_5 with $\Delta E^{0_5\ ZPE}_{seg} = -0.363$ eV vs. -0.278 eV for the site 6 of the perfect GB. In addition, there are two sites O_1 above and below GB_2 with $\Delta E^{0_1\ ZPE}_{seg} = -0.322$ eV. Sites 4' (symmetric of 4, in the structure distorted by the vacancy) and 6' (the perfect GB contains two sites 6, which give 6' and O_5, when the vacancy in introduced) are

Table 2. Positions (in a_0) and segregation energies ΔE^i_{seg} (in eV) obtained by energy minimization with the DFT method for the large (small) GB structures, without vacancy (top table) and with a vacancy on site GB_2 (bottom table). ΔE^{iZPE}_{seg} (in eV) is the segregation energy including the zero point energy correction. The site numbers (i) refer to Fig. 1.

Large (Small) perfect GB					
site i	x	y	z	ΔE^i_{seg}(eV)	ΔE^{iZPE}_{seg}
1	0.921 (0.881)	0.663 (0.669)	0.000 (0.000)	−0.015 (0.000)	−0.033 (0.000)
2	0.033 (0.000)	1.596 (1.600)	0.373 (0.383)	−0.097 (-0.074)	−0.134 (-0.118)
3	0.449 (0.421)	2.017 (2.015)	0.000 (0.000)	−0.110 (-0.072)	−0.123 (-0.078)
4	0.268 (0.227)	1.542 (1.540)	0.500 (0.500)	−0.161 (-0.122)	−0.182 (-0.135)
5	0.024 (0.000)	1.858 (1.853)	0.723 (0.721)	−0.239 (-0.220)	−0.266 (-0.229)
6	**0.024 (0.000)**	**1.109 (1.100)**	**0.000 (0.000)**	**-0.244 (-0.212)**	**-0.278 (-0.222)**
Large (Small) defective GB					
site i	x	y	z	ΔE^i_{seg}(eV)	ΔE^{iZPE}_{seg}
1	0.890 (0.860)	0.668 (0.680)	0.000 (0.000)	0.000 (0.000)	−0.025 (0.000)
2	−0.008 (0.063)	1.669 (1.604)	0.440 (0.410)	−0.160 (-0.151)	−0.210 (-0.186)
3’	0.448	2.019	1.000	−0.079	−0.104
4’	−0.203	1.546	0.455	−0.196	−0.213
5	0.010 (0.000)	1.847 (1.889)	0.708 (0.715)	−0.180 (-0.184)	−0.193 (-0.199)
6	**0.032 (0.014)**	**1.120 (1.124)**	**0.000 (0.000)**	**-0.353 (-0.332)**	**-0.362 (-0.311)**
6’	0.017	1.101	1.000	−0.09	−0.100
O_1	0.254 (0.241)	1.501 (1.500)	0.319 (0.308)	−0.295 (-0.285)	−0.322 (-0.290)
O_2	−0.359 (-0.263)	1.942 (1.865)	0.000 (0.000)	−0.185 (-0.177)	−0.204 (-0.175)
O_3	0.622 (0.617)	1.340 (1.341)	0.000 (0.000)	−0.203 (-0.192)	−0.229 (-0.199)
O_4	0.269 (0.260)	1.866 (1.865)	0.000 (0.000)	−0.294 (-0.281)	−0.314 (-0.279)
O_5	**0.032 (0.014)**	**1.120 (1.124)**	**0.000 (0.000)**	**-0.353 (-0.332)**	**-0.362 (-0.311)**
O_6	0.254 (0.241)	1.501 (1.500)	1.681 (1.715)	−0.295 (-0.285)	−0.322 (-0.290)

minor segregation sites.

3.3. Hydrogen-hydrogen interactions

Large segregation energies, in absolute value, were obtained. It can therefore be anticipated that some sites will be almost fully occupied if the bulk hydrogen concentration is increased at low enough temperature. Mean field equations for isolated site occupancy (ϵ_{ij} set to zero in Eq. 3), show that sites 6, 5 and 4 of the perfect GB are almost saturated, for embrittlement conditions typically used in experiments: c_{bulk} below 1000 ppm and T=300K (Fig. 4). Solute-solute interactions can therefore play a significant role in the H enrichment of the GB, depending on the distance in between these sites. The energetics for this is given by solute-pair interactions [53] ϵ_{ij}. A negative (resp. positive) pair interaction means attraction (resp. repulsion). The calculation of the pairs does not need to be exhaustive. To find which interactions are needed, we step by step increase the bulk concentration are follow the occupancies given by the mean field equations. The deepest traps are sites are 6, 5 and 4 for the perfect GB (resp.

Table 3. Interaction energy between hydrogen atoms (in eV) obtained for the large (small) perfect and defective GB structures. The site numbers (i) refer to Fig. 1. ϵ_{6-i} (in eV) is the pair interaction energy between site number 6 and its neighbors. ϵ_{6-5-i} (in eV) is the three-body interaction energy between the pair (6,5) and its neighbors.

Large(small) perfect GB structure		
site i	ϵ_{6-i}	ϵ_{6-5-i}
2	0.018 (0.004)	0.149 (0.021)
3	−0.012 (-0.012)	−0.025 (-0.025)
4	−0.008 (-0.018)	0.015 (-0.039)
5	−0.001 (-0.018)	—— (——)

Large defective GB structure					
site i	ϵ_{O_5-i}	$\epsilon_{O_5-O_4-i}$	$\epsilon_{O_5-O_4-O_3-i}$	$\epsilon_{O_5-O_4-O_3-5-i}$	$\epsilon_{O_5-O_4-O_3-O_2-5-i}$
2	−0.031	0.002	0.360	0.100	0.246
3	−0.029	0.492	0.361	0.210	0.490
5	−0.002	0.134	−0.036	——	——
O_1	0.045	0.070	0.068	0.169	0.164
O_2	0.032	0.020	0.025	0.010	——
O_3	0.007	−0.010	——	——	——
O_4	−0.030	——	——	——	——

O_5, O_1, O_6 and O_4 in the presence of the vacancy). The first concentration to go up is the one on site 6 (resp. O_5), therefore the pair interaction between a site 6 (resp. O_5) and all the others is calculated first (table 3). The interaction with the next deepest trap site (site 5) is weak, so both sites can be enriched independently. In the vacancy, segregation on O_4 is enhanced by the filling of sites O_5, while it is decreased on sites O_1 and O_6 (table 3). Site O_4 is therefore enriched together with site O_5. The next step is to consider that both sites 6 and 5 (resp. O_5 and O_4) are saturated and evaluate the pair interactions with the other sites. Segregation on site 4 of the perfect GB is only slightly diminished ($\epsilon \sim 0.015$ eV). The other sites will be occupied at concentrations higher than 1000 ppm and therefore are of minor importance for embrittlement. In the vacancy case, sites O_3, 5 and O_2 are consecutively occupied. The corresponding pair interactions are in table 3.

3.4. Grain boundary occupation by hydrogen and vacancies

The preceding sections have shown that the vacancy formation energy on site GB_2 is small. Furthermore, the hydrogen segregation energy to the GB_2 vacancies is strong. It is therefore likely that vacancy-hydrogen clusters (VH_n) form, as previously found in the bulk [35; 37]. The goal is now to calculate the H and VH_n concentrations in the grain boundary. The mean field model presented in section 2.3 can be modified to take into account the VH_n on the GB_2 sites (the one where the vacancy formation energy is the lowest). The new free energy is:

$F_{N_H,V,T}(\{c_i\},\{c_{VH_n}\}) =$

$$
\begin{aligned}
&E_0 + N\ (1 - \sum_{n=0}^{6} c_{VH_n})\ \Big(\sum_i (c_i \Delta E^i_{seg} + \sum_j c_i c_j \epsilon_{ij}) \\
&+ kT \sum_i (c_i \ln c_i + (1 - c_i) \ln(1 - c_i)) \Big) \\
&+ \sum_{n=0}^{n=6} N(c_{VH_n} E_f^{VH_n} + kT c_{VH_n} \ln c_{VH_n}) \\
&+ N\ kT (1 - \sum_{n=0}^{n=6} c_{VH_n}) \ln(1 - \sum_{n=0}^{n=6} c_{VH_n})
\end{aligned} \tag{6}
$$

where N is the number the equivalent GB_2 sites in the system (the number of structural units), n is the number of hydrogen atoms in the VH_n cluster. Note that the label i for interstitial sites designates those interstitial sites which are not inner vacancy sites. Indeed, when a vacancy is created on a GB_2 site, the two sites 4 in first neighbor are replaced by sites O_1 and O_6 of the vacancy, sites 3 and 3' are replaced by sites O_4 and O_2 respectively and site 6 is replaced by site O_5. Sites 5 and 2, which are core interstitial sites of the GB, still exist but are much less attractive than regular vacancy sites. The factor $(1 - \sum_{n=0}^{n=6} c_{VH_n})$, ahead of terms which are function of c_i, is used to mark which of the structural units do not host vacancies and therefore can host hydrogen on regular interstitial sites. There are also two different configurational entropy terms: one for the H atoms on the lattice of the interstitial sites of the structural units free of vacancies and one for the seven VH_n species on the GB_2 plane (one GB_2 per structural unit). The fixed total number of hydrogen atoms $N_H = N(1 - \sum_{n=0}^{n=6} c_{VH_n}) \sum_i c_i + N \sum_{n=0}^{n=6} n c_{VH_n}$ is constrained. Introducing the Lagrange multiplier μ to take into account this constraint and taking the derivative with respect to c_i and c_{VH_n} gives the same equilibrium c_i as Eq. 3, plus the additional relations:

$$
c_{VH_n} = \frac{A_n}{1 + \sum_{j=0}^{6} A_j} \tag{7}
$$

where

$$
A_n = e^{-(E_f^{VH_n} + n\,\mu_H - A\,\mu_H - B)/kT} \tag{8}
$$

with

$$
\begin{aligned}
&A = 0 \qquad \text{if } n = 0 \\
&A = c_2 + 2c_3 + 2c_4 + c_5 + c_6 \qquad \text{if } n \neq 0 \\
&B = c_2 \Delta E^2_{seg} + kT(c_2 \log c_2 + (1 - c_2) \log(1 - c_2)) \\
&\quad + 2(c_3 \Delta E^3_{seg} + kT(c_3 \log c_3 + (1 - c_3) \log(1 - c_3))) \\
&\quad + 2(c_4 \Delta E^4_{seg} + kT(c_4 \log c_4 + (1 - c_4) \log(1 - c_4))) \\
&\quad + c_5 \Delta E^5_{seg} + kT(c_5 \log c_5 + (1 - c_5) \log(1 - c_5)) \\
&\quad + c_6 \Delta E^6_{seg} + kT(c_6 \log c_6 + (1 - c_6) \log(1 - c_6))
\end{aligned} \tag{9, 10}
$$

Ef^{VH_n} is the formation energy of the clusters. As an approximation [37], only one

cluster per class (i.e. per value of n) is taken, with the smallest energy. A list of such formation energies is given in the appendix (table A1).

Figure 2 shows the result for a vacancy formation energy E_f^l of 0.21 eV and a temperature of 300 K. The total number of vacancies is shown with crosses. The detail

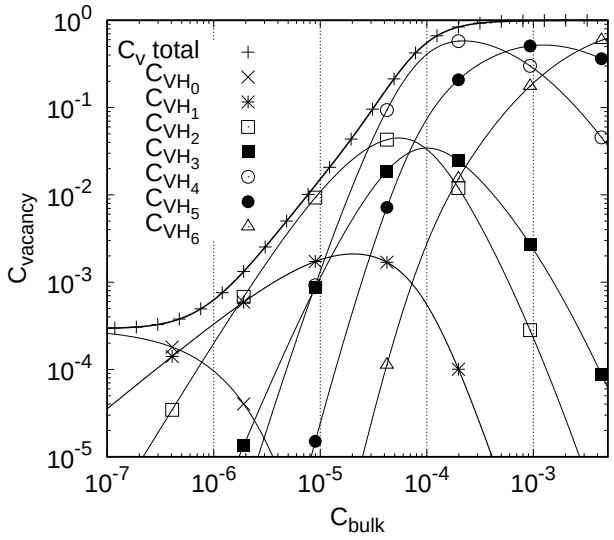

Figure 2. Vacancy-hydrogen clusters concentration on sites GB_2 at T=300K as a function of H bulk concentration. The formation energies of the various clusters are given in the appendix Appendix A.

per cluster is also shown. With these parameters, sites GB_2 are saturated by VH_4 and VH_5 clusters beyond 100 ppm (resp. 1000 ppm at T=400K, Fig. 3, the temperature at which the isolated vacancies start to be mobile in the bulk [38]). Trying to extrapolate to other grain boundaries, the comparison of the VH_n formation energies on site GB_2 of the grain boundary and in the bulk (appendix Appendix A and Table A1) show that the average segregation energy per atom is similar, at least for clusters with 5 and 6 hydrogen. A reasonable model for obtaining the saturation c_{bulk} for a grain boundary, in general, could be to approximate the formation by $E_f^{VH_n} \approx E_f^i + n \times \Delta\overline{E}_{seg}$ with $\Delta\overline{E}_{seg}$ the average segregation energy of the bulk vacancy (-0.26 eV) and E_f^i, the formation energy of the vacancy on site i of the GB. Figure 3 shows that saturation can be obtained, within the c_{bulk} range typical of embrittlement, i.e., below 2000 ppm, only at low temperature (below 400 K) and if E_f^i is low (below 0.5 eV).

The model can be refined further by taking into account the large repulsive interaction between a vacancy and the neighbor sites 6': the segregation energy increases from -0.278 eV up to -0.100 eV (Table 2). The effective, repulsive, pair interaction is therefore $\epsilon_{6-V} = 0.178$ eV. Its variation with the H occupancy of the vacancy is not considered. This effect is included in the mean field model by adding the term $2c_6 \sum_{n=0}^{6} c_{VH_n} \epsilon_{6-V}$ in the free energy (Eq. 6). Then the model predicts a phase transition from a low c_{VH_n} / high c_6 (i.e. high occupancy of regular interstitial sites) phase to a high c_{VH_n} phase at high bulk hydrogen concentration. Figure 4 shows the c_{bulk} value

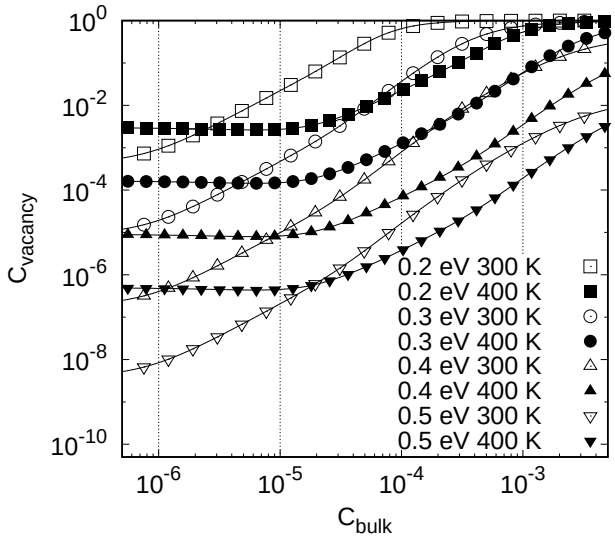

Figure 3. Influence of the vacancy formation energy on the vacancy-hydrogen clusters' concentration at T=300 K (open symbols) and at T=400 K (filled symbols) as a function of bulk concentration.

where these phases separate, close to 40 ppm. Saturation is obtained essentially because of VH_4 and VH_5 clusters (Fig. 4b). In the mean time, the concentration on sites 6 of the structural units which are not occupied by a vacancy, i.e. sites 6' in table 2, drops to almost zero. In addition, we can expect a repulsive interaction between the VH_5 along the tilt axis because of H-H repulsion between sites 5 and the O sites of the second vacancy. One way to avoid this repulsion is to order the vacancies on a checkerboard structure on the GB_2 plane. The maximum occupancy is therefore 50% and the repulsion between the VH_5 and sites 6' and 5' constrains these sites to a low occupancy. Therefore, there are 3 main relevant configurations for the fracture calculations: (i) one corresponds to a segregation in the absence of vacancies (in case vacancy production and diffusion are too slow to reach equilibrium). In this case sites 6 and 5 are fully occupied at c_{bulk} = 100 ppm (T=300K) (see the insert of Fig. 5), i.e. the system contains 8 H, (ii) at c_{bulk} = 1000 ppm (T=300K), sites 4 are occupied at 50%, but there are 2 sites "4" per structural units and therefore the configuration contains 12 H, (iii) a configuration corresponding to the high vacancy concentration where the GB_2 sites are occupied at 50% by VH_5 clusters (configuration 2 VH_5 on Fig. 6).

3.5. Influence on cohesion

In view of these results, the focus is now on the influence of the presence of hydrogen on the cohesion of the grain boundary, with limited diffusion. The situation where the GB is perfect is compared to representative cases where defects are created, with configurations which correspond to experimental conditions, as discussed above. In the simulations, there are four CSL. The cases considered are therefore: one vacancy in or far away from the GB, one VH_5 cluster (25% occupancy of the GB_2 sites), two VH_5 clusters

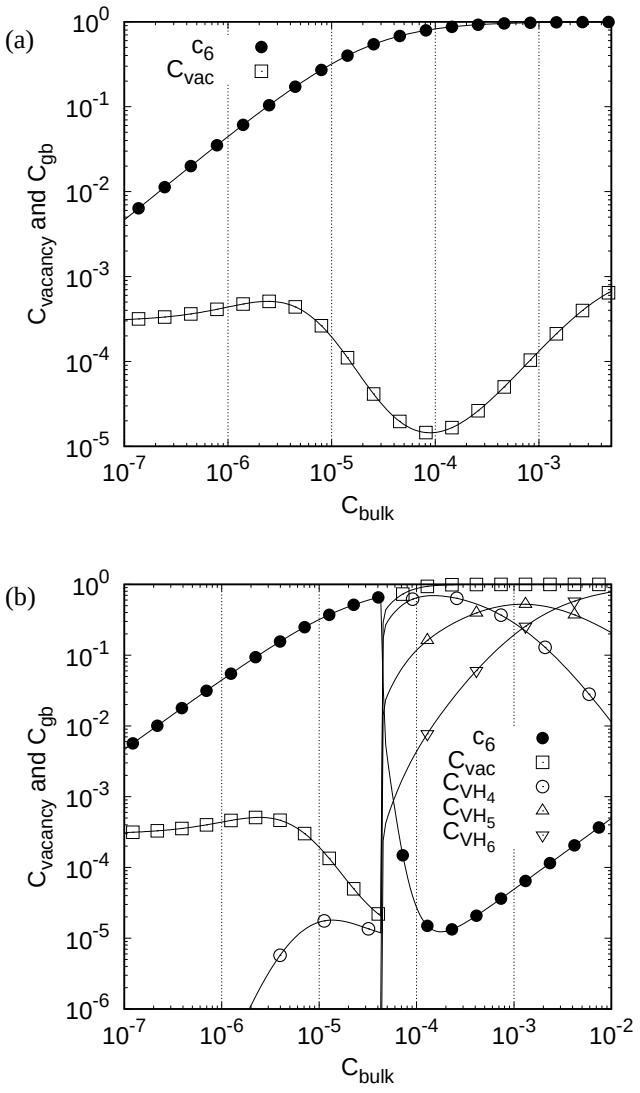

Figure 4. Variation of the hydrogen concentration on site 6 (black points) and of the total vacancy concentration $C_{\rm vac}$ on site GB_2 (open square symbols) given by the mean field model and taking into account the repulsion between vacancies and hydrogen atoms occupying sites 6. (a) (resp. b) shows the low (resp. high) vacancy concentration phase.

in the checkerboard configuration (50% occupancy of the GB_2 sites), and finally, four VH_4 (100% occupancy of the GB_2 sites). Two additional cases were considered. They correspond to the low vacancy phase, where only regular interstitial sites are occupied. The GB was filled with 8 (sites 5 and 6 fully filled) and 12 (sites 4, 5 and 6 filled) H atoms (configuration labeled 8H and 12H below). To carry out the simulations, the Ni atoms were fixed to the edges of the box and the distance between the atoms of the grain boundary was increased. Only the atoms in the vicinity of the fracture (the first Ni planes on either side of the GB and the GB plane itself) were left free to relax, while all H atoms were fully relaxed. The cases with an empty vacancy (in and out the GB)

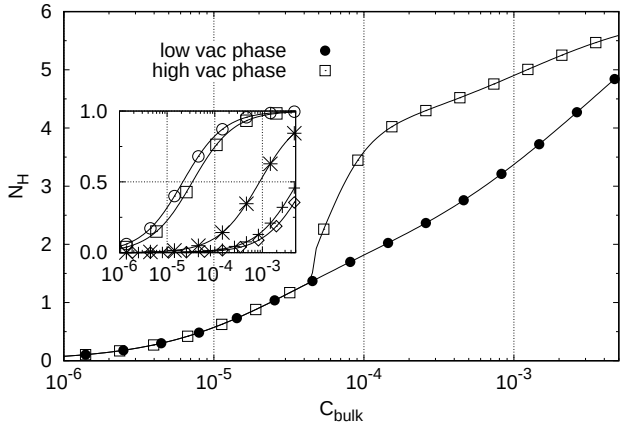

Figure 5. Variation of the total hydrogen content, per structural unit, as a function of the bulk concentration at T=300 K according to Eq. 3 and 7. The insert shows the detail of the occupancy of the sites c_i when the low vacancy phase is enriched in H $c_2(+)$,$c_3(\diamond)$,$c_4(*)$,$c_5(\square)$,$c_6(\circ)$.

are used as control configurations, to see how hydrogen atoms specifically modify the cohesion of the GB. The other cases are the configurations which represent the filled sites for desired experimental concentrations. Figure 6 shows the evolution of the excess energy as a function of the distance between the two slabs.

We first note that the presence of an empty vacancy near the GB does not change the cleavage fracture. The difference in the excess energy between the three configurations (perfect and both cases with a vacancy) is low, smaller than the numerical accuracy. Significant effects appear when H atoms are included in the system. When all favorable interstitial sites are filled with H atoms, i.e. when the system contains 8 or 12 H atoms, the work of fracture decreases by about 25% (Fig. 6a). This value is coherent with the classical difference between surface segregation energy and intergranular segregation energy. The effect is not as clear when vacancy-hydrogen clusters are considered (Fig. 6b), however the maximum slope of the curve markedly decreases as a function of the number of vacancy-hydrogen clusters in the system. This slope, evaluated by the numerical gradient of the data in Fig. 6, is taken as an estimate of the cohesive stress σ_{max} and reported in table 4. It decreases from 23 GPa in the "pure Ni" case, i.e. the case where the GB carries no hydrogen and no defects, to 20 GPa (13% drop) in the case of hydrogen segregation only (i.e. configurations 8H and 12H in Fig. 6a) and to 14 GPa when the interface is saturated with VH_4 clusters (40% drop). In this last case, the work of fracture is higher than any other case, and even higher than the perfect GB. This is because the breaking procedure is quasi-static with a very low temperature which does not anneal the surface. It generates a high energy surface state. It was checked that the conclusions regarding embrittlement are not changed when the work of fracture is diminished to represent an annealed surface (see table 4).

The calculations show that the presence of hydrogen qualitatively decreases cohesion, either by decreasing the work of fracture or the cohesive stress, but we would

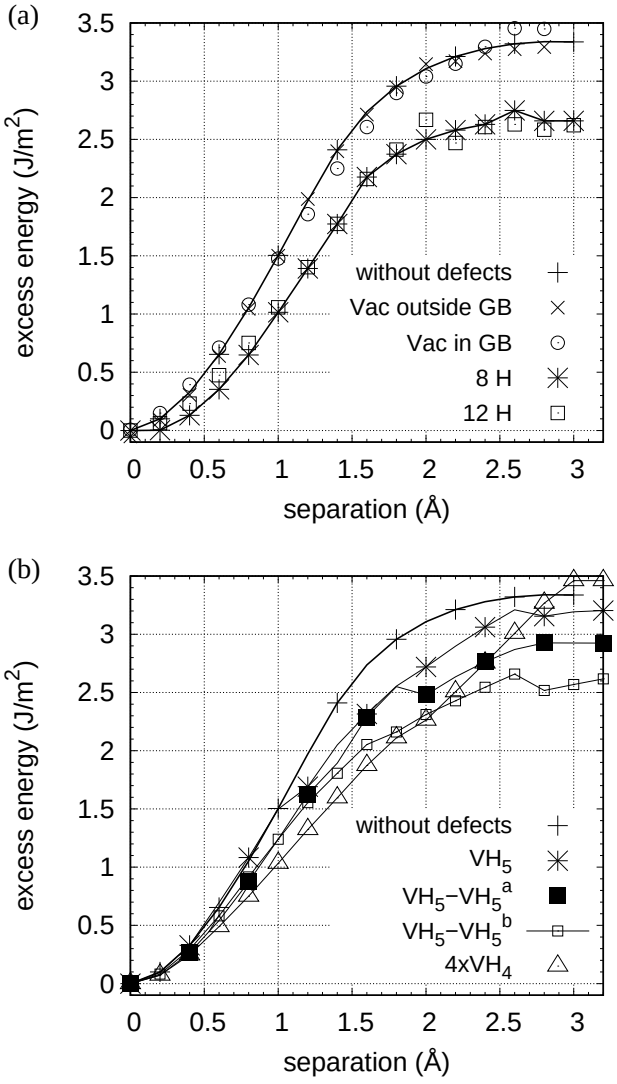

Figure 6. Excess energy versus separation curve: (a) comparison between the GB without defects, with a single vacancy and the GB with segregated hydrogen (eight or twelve hydrogen atoms, without vacancies), (b) influence of vacancy hydrogen clusters. Different cases were considered: the perfect GB, the GB with one VH_5, two VH_5 or four VH_4 clusters. In $VH_5 - VH_5^a$ (resp. $VH_5 - VH_5^b$), the vacancies are on the same (resp. opposite) side of the GB.

like to go further by quantifying the embrittlement of the immediate vicinity of the crack tip. This is done by considering the competition between crack propagation and dislocation emission from the tip (intrinsic ductility). In a previous work dealing with the impact of nanocavities on fracture [54], it was shown, by comparison with classical atomistic simulations of cracks, that a cohesive zone model, with parameters taken from atomistics, can be used to quantify this competition. This model is used again here with parameters obtained from the work of fracture W and the cohesive stress σ_{max} and presented in table 4. It was shown (article [54] and its supplemental material) that the crack opening profile, at least when some damage develops in the

Table 4. The table gives the cohesive stress σ_{max} (GPa) obtained from the gradient of the energy in Fig. 6, the critical opening δ_c (nm), the work of fracture W (Fig. 6) and the maximum displacement shift $\Delta\tilde{u}_z$ (nm) [54]. In parenthesis, in the last column, are the parameters taken to evaluate the impact of a lower work of fracture that could be obtained if the fracture surface was annealed. The impact on $\Delta\tilde{u}_x$ is small: it decreases from 0.044 to 0.040 nm. The threshold for embrittlement is 0.035 nm.

system	Pure Ni	8H-12H	1 VH_5	VH_5-VH_5 $_a$	VH_5-VH_5 $_b$	4 VH_4
σ_{max} (GPa)	23	20	21	21	17	14
δ_c^* (nm)	0.30	0.27	0.30	0.27	0.30	0.50 (0.30)
W (J/m^2)	3.35	2.70	3.20	2.90	2.60	3.45 (2.10)
max $\Delta\tilde{u}_z$ (nm)	0.061	0.053	0.056	0.055	0.047	0.044 (0.040)

fracture process zone, can be accurately modeled by a simple triangular cohesive law: $\sigma(\delta) = \sigma_{max}(1 - \delta/\delta_c)$, where δ is the opening (twice the displacement in the direction perpendicular to the crack plane, i.e. the x direction in Fig. 1) and δ_c is the critical opening beyond which the cohesive stress $\sigma(\delta)$ is zero. δ does not include the elastic part of the displacement and is zero beyond the end of the fracture process zone where the elastic behavior is recovered. In the early stage of fracture, or if the structure does not reorganize during fracture like during cleavage cracking, the UBER model [23; 55] is more appropriate. With this triangular law, the critical opening is obtained by the relation $W = 1/2 \times \sigma_{max} \times \delta_c$. It is of the order of 0.3 nm (table 4). Away from the fracture process zone, the system is elastic with the Voigt average elastic constants (isotropic) $\mu = 94.7$ GPa and $\nu = 0.276$ for Ni ([56] p. 835). The problem to be solved here is an internal crack, in an infinite elastic medium, submitted to a remote applied stress, with a nonlinear cohesive zone ahead of each crack tip. It was solved within the infinitesimal dislocation density formalism [54]. For every applied stress, the fracture process zone length L_{pz} and the crack opening profile $\delta(y)$ were calculated. Upon increasing the applied load, the stiff fracture process zone forces the crack to bow out, inducing a localized shear in the vicinity of the crack tip. It is characterized by the displacement shift $\Delta\tilde{u}_x$ which is the projection, in the direction of easy glide, of the difference in displacement of two atoms in first neighbor position on the surface. $\Delta\tilde{u}_x$ is maximum in the vicinity of the tip. As the mechanical load increases, this maximum first increases up to a maximum value and then decreases (Fig. 7). Appendix B shows representative crack opening profiles and $\Delta\tilde{u}_x$ profiles from which the data in Fig. 7 were obtained. For every configuration of the interface (pure Ni, segregated hydrogen, or various concentrations of vacancy-hydrogen clusters) the maximum value of the curve represents the maximum shear localization the crack tip undergoes during mechanical loading. This value is reported in table 4. It decreases from 0.061 nm down to 0.053 nm when segregated hydrogen is introduced in the system and then further down to 0.044 nm when the concentration of vacancy hydrogen clusters is set to its maximum (corresponding to 4 VH_4 clusters i.e. 100% occupancy of the GB_2 sites in the interface). This represents a drop by 28%. In the case of nanocavities in Al, it was shown in [54] that

dislocation emission corresponds to a fairly low value of $\Delta\tilde{u}_x$, of the order 0.04 nm in the case of Al (approximately one half of the glide necessary to reach the unstable stacking configuration). Rescaling this value to take into the difference of lattice parameter between Al and Ni brings this threshold to 0.035 nm. This value corresponds to a massive drop of 43% with respect to the perfect GB, while the maximum drop of $\Delta\tilde{u}_x$ is only of 28% in the best case of the VH_4 clusters. As a consequence, even if the presence of hydrogen, and even more in the presence of vacancy-hydrogen clusters, decreases the maximum value $\Delta\tilde{u}_x$, it is always much higher than the threshold. Therefore the tip will emit dislocations upon mechanical loading.

The conclusion is that even if the presence of hydrogen and vacancies very significantly weakens the interface in such a way that the fracture process zone is less stiff (the crack opening profile is less steep), dislocations will still be emitted from the tip upon mechanical loading. This will induce blunting and shielding which prevents the full development of the fracture process zone and ultimately the initiation of crack propagation. In appendix Appendix B, more details about the way $\Delta\tilde{u}_x$ is calculated are given. In particular, two crack orientations and three slip systems were tested. They all remain ductile according to the model.

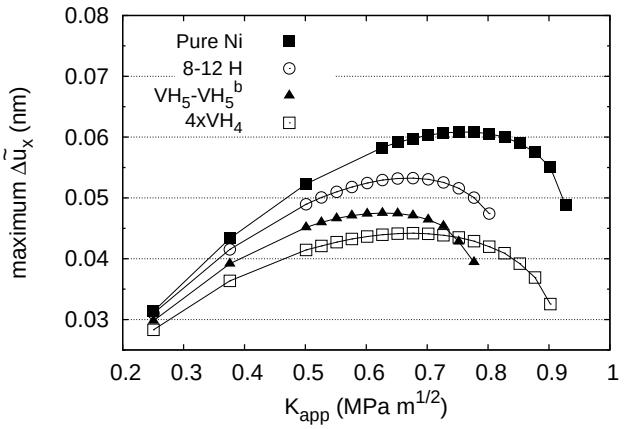

Figure 7. Evolution of the maximum displacement shift $\Delta\tilde{u}_x$ as a function of the applied stress intensity factor K_{app} for different GB cases referred to in Fig. 6 and in table 4. The "pure Ni" case is the GB without hydrogen and without defects. These values are obtained for the most brittle crack / slip system orientation studied: a crack front parallel to [001] (with a crack propagation direction along $[1\overline{2}0]$ and the slip system $(1\overline{1}1)[121]$.

4. Conclusion

Realistic configurations for the $\Sigma5(210)[001]$ symmetrical grain boundary, in Ni containing hydrogen and vacancies, were simulated. The basic energetic parameters, such as the intergranular segregation energy, the H-H pair interaction energy and the vacancy-hydrogen cluster formation energies were calculated by DFT. Then a mean

field model was constructed to find which configurations are the most probable, at equilibrium, as a function of bulk hydrogen concentration and temperature. Two typical structures emerged from this analysis: one with only intergranular hydrogen, at a concentration of 2 hydrogen atoms per structural unit without vacancies and another one with 50% of VH_5 clusters (configuration $VH_5 - VH_5^{a,b}$), which corresponds to 2.5 hydrogen atoms per structural unit (at 1000 ppm H in the bulk and 300 K). The limitation of the enrichment of the interface with H comes from, on the one hand, a repulsion between the VH_5 clusters by overlap of H positions, which limits their concentration to 50%, and on the other hand, a repulsion between the vacancy and the sites 5 and 6 of the nearest structural unit free of vacancies (sites 5 and 6'). This involves that a vacancy hydrogen cluster is not surrounded by segregated hydrogen.

Both structures were fractured in DFT. They show a similar reduction of the ideal work of fracture, but a lower cohesive stress is found in the presence of vacancies (configuration $VH_5 - VH_5^b$). This tendency is confirmed by the fracture behavior of a configuration saturated with VH_4 clusters (1 cluster per structural unit). The embrittlement effect was quantified by calculating the intensity of the shear localization at the crack tip. It was concluded that the decrease of the cohesion of the GB is too limited to prevent dislocation emission at the crack tip. Therefore the "damage" considered in this paper is not sufficient to embrittle the $\Sigma5(210)[001]$ GB in Ni, in conditions of H concentration typical of experiments where intergranular cracks are observed. Further work will be dedicated to other forms of damage, in particular time dependent, in line with the study of nanocavities in [54].

5. Acknowledgments

This work is supported by l'Agence Nationale de la Recherche (ANR) under grant *EcHyDNA* (Blanc 1019424). This work was granted access to the HPC resources from CALMIP (Toulouse, France, Grant 2018-p0749) and PSMN at the ENS de Lyon. CNRS (INP) is also gratefully acknowledged for additional funding.

Appendix A.

The formation energy of the various VH_n configurations, on sites GB_2, are given in table A1. They are obtained from the data in tables 2 and 3, following the expression $E_f^{VH_n} = E_f^{VH_{n-1}} + \Delta E_{seg}^i + \epsilon_{VH_{n-1}-i}$.

Appendix B.

Figure A1 shows the crack opening profiles $\delta(y)$ which correspond to the mechanical equilibrium of an internal crack with nonlinear fracture process zones described by the triangular traction/opening relation presented in subsection 3.5. The profiles are converted into localized shear by computing the finite difference $\Delta\tilde{u}_x = \cos\alpha[u_x(y) -$

Table A1. Vacancy-hydrogen cluster formation energy $E_f^{VH_n}$ and average segregation energy per hydrogen atom, as a function of n, the number of hydrogen in the vacancy. For comparison, the value for the bulk vacancy is also given [37].

n	configuration	$E_f^{VH_n}$ (eV)	$\Delta\overline{E}_{seg}$ (eV)
0	——	0.21	——
1	O_5	−0.152	−0.362
2	O_5O_4	−0.496	−0.353
3	$O_5O_4O_3$	−0.735	−0.315
4	$O_5O_4O_35$	−1.037	−0.312
5	$O_5O_4O_35O_2$	−1.231	−0.288
6	$O_5O_4O_35O_2O_1$	−1.384	−0.265
6	bulk	——	−0.263

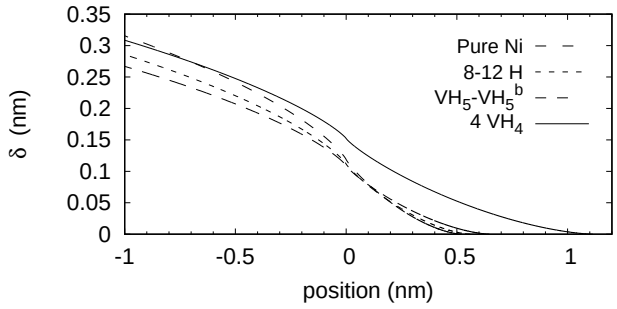

Figure A1. Crack opening profiles δ (nm) corresponding to four structures: GB without defects ("Pure Ni"), GB with segregated hydrogen ("8-12 H"), GB with vacancy-hydrogen clusters ("VH_5-VH_5^b" and "4 VH_4"). The loads correspond to the maximum of shear localization at the tip, i.e. respectively 0.75 MPam$^{1/2}$, 0.68 MPam$^{1/2}$, 0.63 MPam$^{1/2}$ and 0.68 MPam$^{1/2}$.

$u_x(y+\Delta y)]$, where Δy is the distance between two atomic rows on the crack surface and $u_x(y) = \delta(y)/2$ is the displacement perpendicular to the crack plane at position y. α is the angle between the normal to the crack plane and the glide direction (the Burgers vector). Δy is related to the distance between glide planes d_0 by $\Delta y = d_0 \cos\phi/\cos\alpha$, where ϕ is the angle between the trace of the slip plane in the crack plane and the crack front. Two crack orientations were tested. The first one has a crack front along $[1\overline{2}0]$ and a propagation direction along [001] (the tilt axis of the GB). The slip system studied, in interaction with this crack, is $(111)[11\overline{2}]$, with parameters $\cos\phi/\cos\alpha = 1.65$ and $\cos\alpha = 0.55$. The second crack orientation has a crack front along [001] and a propagation direction direction along $[1\overline{2}0]$. It is orthogonal to the previous one. Two slip systems were considered: $(1\overline{1}1)[21\overline{1}]$ ($\cos\phi/\cos\alpha = 0.87$ and $\cos\alpha = 0.92$) and $(1\overline{1}1)[121]$ ($\cos\phi/\cos\alpha = 1.09$ and $\cos\alpha = 0.73$). The three crystallographic configurations have very similar $\Delta\tilde{u}_x$ profiles, the last one being the most brittle. Examples of $\Delta\tilde{u}_x$ profiles, for this crack/slip system orientation, are given on figure B1. The peak values are reported in Fig. 7, as a function of the applied mechanical load.

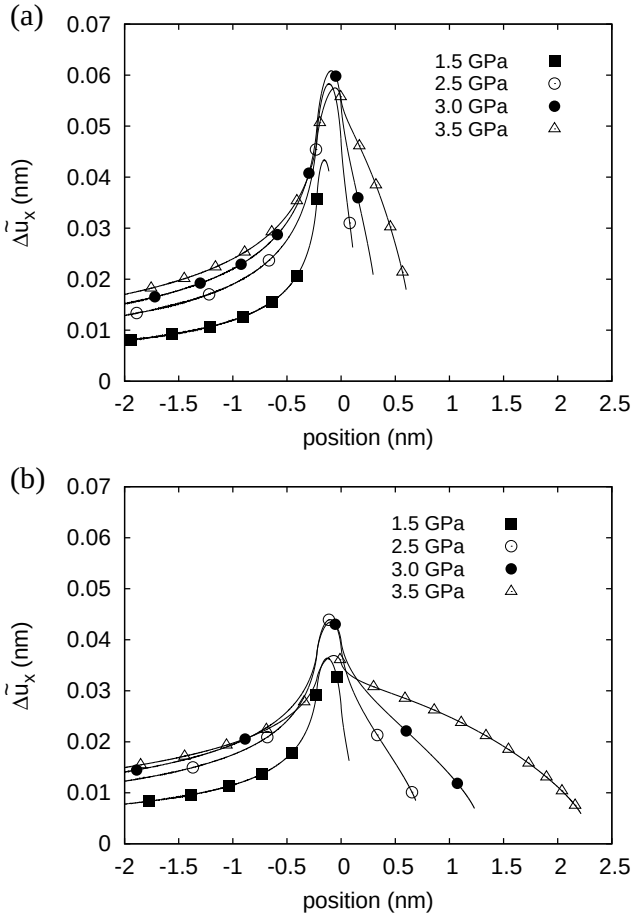

Figure B1. Displacement shift profiles $\Delta\tilde{u}_x$ for different mechanical loads applied to the GB (a) without any defect ("pure Ni" configuration) and (b) saturated with VH_4 clusters. The crack front is [001], the propagation direction is $[1\overline{2}0]$ and the slip system is $(1\overline{1}1)[121]$ ($\Delta_y = 0.22$ nm).

References

[1] Gangloff R and Somerday B (eds) 2012 *Gaseous hydrogen embrittlement of materials in energy technologies* vol 1 (Woodhead Publishing)

[2] Vehoff H and Rothe W 1983 *acta metallurgica* **31** 1781–1793

[3] Xie D, Li S, Li M, Wang Z, Gumbsch P, Sun J, Ma E, Li J and Shan Z 2016 *nat. comm.* **7** 13341

[4] Gruhl W 1984 *Zeitschrift Für Metallkunde* **75** 819–826

[5] Tiegel M C, Martin M L, Lehmberg A K, aind C Borchers M D and Kirchheim R 2016 *acta materialia* **115** 24–34

[6] Wan D, Deng Y and Barnoush A 2018 *Scripta. Mater.* **151** 24–27

[7] Lynch S 2013 *Metallurgical and Materials Transactions A* **44A** 1209

[8] Birnbaum H, Buckley C, Zeides F, Sirois E, Rozenak P, Spooner S and Lin J 1997 *Journal Of Alloys And Compounds* **253** 260–264

[9] Lii M J, Chen X F, Katz Y and Gerberich W W 1990 *acta metall. mater.* **12** 2435

[10] Katz Y, Tymiak N and Gerberich W 2001 *Eng. Frac. Mech.* **68** 619–646

[11] Robertson I 2001 *Engineering Fracture Mechanics* **68** 671 – 692

[12] Girardin G, Huvier C, Delafosse D and Feaugas X 2015 *acta mater.* **91** 141–151

[13] Aubert I, Saintier N, Olive J M and Plessier F 2016 *acta mater.* **104** 9–17

[14] Yu H, Cocks A and Tarleton E 2019 *J. Mech. Phys. Solids* **123** 41–60

[15] Fukai Y 2003 *The Metal-Hydrogen System: Basic Bulk Properties* (Springer-Verlag Berlin and Heidelberg GmbH & Co. K; 2nd edition)

[16] Nagumo M 2004 *Materials Science and Technology* **20** 940

[17] Takahashi J, Kawakami K, Kobayashia Y and Tarui T 2010 *Scripta Mater* **63** 261

[18] Martin M L, Somerday B P, Ritchie R O, Sofronis P and Robertson I M 2012 *Acta Materialia* **60** 2739–2745

[19] Robertson I M, Sofronis P, Nagao A, Martin M, Wang S, Gross D and Nygren K 2015 *Metallurgical and materials transaction A* **46A** 2323–2341

[20] Deng Y and Barnoush A 2018 *acta mater.* **142** 236–247

[21] Hribernik M L 2006 *Cleavage Oriented Iron Single Crystal Fracture Toughness* PhD thesis under the supervision of G. R. Odette UC Santa Barbara

[22] Wan D and Barnoush A 2019 *Mat. Sci. Eng. A* **744** 335–339

[23] Möller J J, Mrovec M, Bleskov I, Neugebauer J, Hammerschmidt T, Drautz R, Elsässer C, Hickel T and Bitzek E *Phys. Rev. Mat.* **2** 093606

[24] Zamora R J, Nair A K, Hennig R G and Warner D H 2012 *Phys. Rev. B* **86** 060101(R)

[25] Sun Y, Peng Q and Lu G 2013 *Phys. Rev. B* **88** 104109

[26] Wang Y, Connétable D and Tanguy D 2019 *Phil. Mag.* **99** 1184–1205

[27] Kirchheim R 1988 *Progress in Materials Science* **32** 261–325 ISSN 0079-6425

[28] Du Y A, Rogal J and Drautz R 2012 *Phys. Rev. B* **86** 174110

[29] Di Stefano D, Mrovec M and Elsässer C 2015 *acta mat.* **98** 306–312

[30] Zhou X, Mousseau N and Song J 2019 *Phys. Rev. Lett.* **122** 215501

[31] Wang Y, Connétable D and Tanguy D 2019 *Phil. Mag.* **99** 1184–1205

[32] Subramanyam A P A, Guzm'an A A, Vincent S, Hartmaier A and Janisch R 2019 *Metals* **9** 291

[33] McEniry E J, Hickel T and Neugebauer J 2018 *acta mater.* **150** 53–58

[34] Tateyama Y and Ohno T 2003 *Phys. Rev. B* **67** 174105

[35] Nazarov R, Hickel T and Neugebauer J 2014 *Phys. Rev. B* **89** 144108

[36] Ismer L, Park M S, Janotti A and Van de Walle C G 2009 *Phys. Rev. B* **80** 184110

[37] Tanguy D, Wang Y and Connétable D 2014 *acta mat.* **78** 135–143

[38] Wang Y, Connétable D and Tanguy D 2015 *Phys. Rev. B* **91** 094106

[39] Wang Y, Connétable D and Tanguy D 2016 *acta mater.* **103** 334–340

[40] Song J and Curtin W 2011 *acta mater.* **59** 1557–1569

[41] Rice J R and Wang J 1989 *Materials Science and Engineering* **A 107** 23–40

[42] Van der Ven A and Ceder G 2004 *acta mater.* **52** 1223–1235

[43] Tehranchi A, Zhou X and Curtin W 2020 *acta mater.* **185** 98–109

[44] Tehranchi A and Curtin W A 2017 *J. Mech. Phys. Solids* **101** 150–165

[45] Momida H, Asari Y, Nakamura Y, Tateyama Y and Ohno T 2013 *Phys. Rev. B* **88** 144107

[46] Takai K, Shoda H, Suzuki H and Nagumo M 2008 *acta materialia* **56** 5158–5167

[47] Perdew J, Burke K and Ernzerhof M 1996 *Phys. Rev. Lett.* **77** 3865

[48] Kresse J and Hafner J 1993 *Phys. Rev. B* **47** 558

[49] Kresse G and Joubert D 1999 *Phys. Rev. B* **59** 1758

[50] Connétable D, Wang Y and Tanguy D 2014 *Journal of Alloys and Compounds* **614** 211–220

[51] Gong Y, Grabowski B, Glensk A, Körmann F, Neugebauer J and Reed R C 2018 *Phys. Rev. B* **97** 214106

[52] Alvaro A, Jensen I T, Kheradmand N, Løvvik O and Olden V 2015 *Int. J. Hydrogen Energy* **40** 16892–16900

[53] Shen X J, Tanguy D and Connétable D 2014 *Philos. Mag.* **94** 2247–2261

[54] Tanguy D 2017 *Phys. Rev. B* **96** 174115

[55] Janisch R, Ahmed N and Hartmaier A 2010 *Phys. Rev. B* **81** 184108

[56] Hirth J P and Lothe J 1992 *Theory of Dislocations, 2nd edition* (Krieger Pub Co)